

Detection of a Far IR Excess with DIRBE at 60 and 100 Microns

Douglas P. Finkbeiner & Marc Davis

University of California at Berkeley, Departments of Physics and Astronomy, 601 Campbell Hall, Berkeley, CA 94720

and

David J. Schlegel

Princeton University, Department of Astrophysics, Peyton Hall, Princeton, NJ 08544

ABSTRACT

From analysis of the DIRBE weekly averaged sky maps, we have detected substantial flux in the $60\mu\text{m}$ and $100\mu\text{m}$ channels in excess of expected zodiacal and Galactic emission. Two methods are used to separate zodiacal light from more distant emission. Method I makes use of the time-dependence of the North-South annual variation observed at the ecliptic poles. This method is robust against errors in the inter-planetary dust (IPD) model, but does not demonstrate isotropy of the background. Method II measures the ecliptic latitude dependence of the dust over a range of ecliptic latitudes ($|\beta| > 35^\circ$) at solar elongation $e = 90^\circ$. This allows the excess to be determined in each week of the DIRBE mission for high redundancy, but the results depend weakly on the IPD model. Both methods give consistent results at $60\mu\text{m}$ and $100\mu\text{m}$. The observed signal is consistent with an isotropic background at the level $\nu I_\nu = 28.1 \pm 1.8 \pm 7(\text{syst}) \text{ nW m}^{-2}\text{sr}^{-1}$ at $60\mu\text{m}$ and $24.6 \pm 2.5 \pm 8 \text{ nW m}^{-2}\text{sr}^{-1}$ at $100\mu\text{m}$.

The IR excess detected at 140 and $240\mu\text{m}$ by these methods agrees with previous measurements, which are thought to be the cosmic infra-red background (CIB). The detections at 60 and $100\mu\text{m}$ are new. The integrated IR excess in the window $45 - 125\mu\text{m}$ is $23 \pm 8 \text{ nW m}^{-2}\text{sr}^{-1}$, to be added to the $18 \pm 4 \text{ nW m}^{-2}\text{sr}^{-1}$ previously measured with the DIRBE and FIRAS instruments in the window $125 - 2 \text{ mm}$. While this new excess is not necessarily the CIB, we have ruled out all known sources of emission in the solar system and Galaxy. We therefore tentatively interpret this signal as the CIB and consider the implications of such energy production from the viewpoint of star formation efficiency and black hole accretion efficiency. However, the IR excess exceeds limits on the CIB derived from the inferred opacity of the IGM to observed TeV photons, thus casting doubt on this interpretation. There is currently no satisfactory explanation for the $60 - 100\mu\text{m}$ excess.

Subject headings: cosmology: observations — diffuse radiation — infrared: ISM: continuum — interplanetary medium — galaxies: active — gamma rays: observations

1. INTRODUCTION

The extra-galactic background light (EBL), from optical to sub-millimeter wavelengths, records the energetics history of galaxy formation. This background is the cosmic relic of star formation, AGN, and black hole formation. The existence of such a background was discussed first in the optical and near IR (Partridge & Peebles 1967) and then at other wavelengths (Low & Tucker 1968; Peebles 1969; Harwit 1970; Kaufman 1976; Dube et al. 1979). However, measurement of an unresolved background is very difficult at most wavelengths because of numerous foregrounds which may be many times brighter. Direct measurement of the individual background sources by deep, high resolution imaging has only recently become possible, and only at selected wavelengths.

1.1. Current Knowledge of Extragalactic Background

The Infra-Red Astronomical Satellite (*IRAS*) in 1983 obtained the first full-sky census of far infrared (FIR) point sources. Some 300,000 point sources, including $\sim 20,000$ galaxies, were detected in four bands from $12 - 100\mu\text{m}$ (see Beichman et al. 1988). Optical follow-up indicated that typically 30% of the bolometric luminosity of these galaxies is radiated in the FIR (Soifer & Neugebauer 1991), presumably as thermal radiation from dust heated by optical/UV radiation. In the case of ultra-luminous IR galaxies (ULIRGs) up to 95% of the bolometric luminosity is radiated in the FIR (e.g., Sanders & Mirabel 1996), suggesting that optically obscured galaxies might produce a substantial fraction of the extragalactic background light. Mid IR ($12 - 25\mu\text{m}$) emission from most ULIRGs is centrally concentrated, consistent with AGN activity (Soifer et al. 1999).

More recently, Puget et al. (1996) used the *COBE* Far InfraRed Absolute Spectrophotometer (FIRAS) data to constrain the FIR/SMM background at longer wavelengths. They found that the integrated energy of the EBL in the $200\mu\text{m} - 2\text{mm}$ window is comparable to that emitted at optical/near IR wavelengths. This picture was confirmed by Guiderdoni et al. (1997) who concluded that the majority of high- z star formation may be hidden by dust. The FIRAS measurement was greatly refined by Fixsen et al. (1998) who obtained a fit to the CIB of the form

$$I_\nu = (1.3 \pm 0.4) \times 10^{-5} (\nu/\nu_0)^{0.64 \pm 0.12} B_\nu(18.5 \pm 1.2 \text{ K}) \quad (1)$$

in the interval $150 < \nu < 2400$ GHz ($2000 - 125\mu\text{m}$), where $\nu_0 = 3000$ GHz and $B_\nu(T)$ is the Planck function. The integrated intensity observed in this frequency interval is 14 ± 4 nW m⁻²sr⁻¹. This curve is the dotted line shown in Figure 1.

Recent efforts to resolve this background into discrete sources with the SCUBA detector on the James Clerk Maxwell Telescope have been very successful (Smail et al. 1997; Hughes et al. 1998; Barger et al. 1998; Eales et al. 1999). By extending the counts to a limit of 0.5 mJy in cluster-lensed fields, enough counts are found to account for most of the expected 850 μm background of $\nu I_\nu = 5 \pm 2 \times 10^{-1}$ nW m⁻²sr⁻¹ (Blain et al. 1999b).

At shorter wavelengths, the background is not resolvable with current instruments, and zodiacal emission from interplanetary dust (IPD) hampers detection of the unresolved background. The zodiacal emission peaks at $\sim 25\mu\text{m}$ and dominates any expected signal from the CIB in most DIRBE channels. Nevertheless, the background has been measured at 140 μm and 240 μm by Schlegel, Finkbeiner, & Davis (1998). A more thorough analysis by the DIRBE team (Hauser et al. 1998) improved those results, and also provided upper limits in the other 8 DIRBE channels (see Figure 1). The FIRBACK survey at 175 μm (Puget et al. 1999) using the *Infrared Space Observatory (ISO)* detected point sources to a flux limit of 200 mJy, yielding an integrated flux significantly higher than a simple extrapolation of IRAS counts would have predicted, but still much lower than the observed background. Puget et al. (1999) claim that a plausible extrapolation of the counts down to 10 mJy would account for the entire background at 175 μm .

At wavelengths $\lambda \leq 3.5\mu\text{m}$, emission from Galactic stars dominates that from zodiacal dust. Using ground-based 2.2 μm counts to remove the stellar foreground, and adopting a value of 7.4 nW m⁻²sr⁻¹ at 2.2 μm , Dwek & Arendt (1998) measured the background at 3.5 μm to be $\nu I_\nu \sim 10 \pm 3$ nW m⁻²sr⁻¹. Gorjian, Wright, & Chary (1999) make different assumptions about the stellar foregrounds, yet arrive at a similar result: 16.2 ± 6.4 nW m⁻²sr⁻¹ at 2.2 μm and 9.3 ± 3 nW m⁻²sr⁻¹ at 3.5 μm .

At optical wavelengths the Hubble Space Telescope can resolve a large fraction of the extragalactic background. By integrating the light of the resolved galaxies in the HDF, Pozzetti et al. (1998) find that the brightness of the extragalactic sky is $2.1_{-0.3}^{+0.4} \times 10^{-20}$ erg cm⁻²s⁻¹Hz⁻¹sr⁻¹ in I-band ($\sim 0.8\mu\text{m}$), which is equivalent to $\nu I_\nu = 8$ nW m⁻²sr⁻¹. In the other Hubble broadband filters, this background obeys $\nu I_\nu \sim \nu^{-1}$ for 2000 - 8000Å. The HDF counts in each filter appear to flatten at the faint end, indicating a possible convergence, although other authors find hints of an optical/UV background as much as twice this large (Bernstein 1997). Comparing the latest FIR background with the optical/UV background has supported the view that $\sim 2/3$ of the starlight in high- z galaxies is reprocessed by dust into FIR radiation, a much higher

percentage than in local galaxies. Where, then, are the sources of the FIR background?

It is well established that the ULIRGs are typically interacting galaxies (see Sanders & Mirabel 1996), and Williams et al. (1996) find that most high- z objects in the HDF are interacting. What is not very well established is the dominant energy source in these objects, especially at the high-luminosity end. Certainly, many of these objects are powered by starbursts; only the very brightest objects so far observed are primarily powered by AGN (Genzel et al. 1998, Lutz et al. 1998). But this scenario may change at high redshift. Measurements of the X-ray background provide some constraint on AGN activity, unless the very brightest AGN are so obscured that even 10 keV photons cannot escape.

1.2. Interpretation

The above observational evidence allows for a coherent interpretation. Interacting ULIRGs at high- z undergo violent episodes of dusty star formation, with AGN as a minor contributor to the energy. Roughly 2/3 of this energy is reprocessed to the FIR. Accounting for present day metallicity of galaxies and the IGM enrichment, the energy from stars allows for an integrated extragalactic background light (EBL) of $I_{\text{bol}} = 50/(1 + z_f)$ nW m⁻²sr⁻¹ (see §5.1), which is roughly consistent with current measurements if the formation redshift $z_f \lesssim 2$.

The IR excess measurements presented in this paper, if they are interpreted as an extragalactic background, would push this paradigm to the limit. They would indicate an integrated EBL flux in the far IR of ~ 40 nW m⁻²sr⁻¹ with a hot spectrum, possibly suggesting that AGN dominate the energy input in early galaxies, at least at short wavelengths. This interpretation might also imply the presence of up to $\sim 0.15\%$ of all baryons in black holes, and possibly violate constraints on the X-ray background. Furthermore, recent measurements of high energy gamma rays place limits on the opacity of the IGM, which is primarily due to pair production on CIB photons. The interpretation of the 60 – 100 μ m excess as CIB raises serious problems; however, we have been unable to identify any alternative source in the Galaxy, local bubble, or Solar system that can account for the emission.

1.3. Organization of Paper

We review previous foreground models in §2, and present our two procedures for extracting the IR excess signal in §3. Our assessment of various systematic errors is given

in §4. In §5 we discuss the energy crisis resulting if this emission is interpreted as an extragalactic background. In addition, we discuss the constraint on the density of CIB photons implied by the observation of TeV photons from nearby AGN. These difficulties, as well as general conclusions and prospects for the future appear in §6.

2. FOREGROUNDS

2.1. Zodiacal Emission

The main difficulty in measuring the CIB at $60 - 240\mu\text{m}$ is contamination from zodiacal light, which is thermal emission from the interplanetary dust (IPD). This emission is brightest in the DIRBE 12 and $25\mu\text{m}$ bands, falling approximately as a blackbody at longer wavelengths. The emission at the ecliptic poles is $\nu I_\nu \sim 260$ and $50 \text{ nW m}^{-2}\text{sr}^{-1}$ in the DIRBE 60 and $100\mu\text{m}$ bands respectively (Fig. 1). Emission in the ecliptic plane is $\sim 3 - 4$ times brighter. This emission must be carefully removed in order to measure the much fainter extragalactic background.

The IPD cloud is difficult to model, especially at low ecliptic latitude. At high latitude, one looks through dust in the neighborhood of the Earth, but at low latitude, the situation is more complex: the dust density and temperature vary significantly along a line of sight, several distinct dust rings are seen, and a density resonance in the Earth’s orbit is observed. These factors make it nearly impossible to model the zodiacal light at low latitudes from $5 - 100\mu\text{m}$. Furthermore, temperature and density variations appear even in the near-Earth dust, beyond the expected variation due to changes in the Earth-Sun distance through the year.

2.1.1. SFD98 Zodiacal Emission Model

A simple approach to the problem of separation of zodiacal light from other emission is presented in Schlegel, Finkbeiner, & Davis (1998; hereafter SFD98). They use the $25\mu\text{m}$ map as a spatial template of the zodiacal light. At high ecliptic latitude, most of the dust is less than 0.4 AU from Earth and has a fairly uniform temperature. Near the ecliptic plane, one sees dust of varying temperature out to several AU. Therefore, this $25\mu\text{m}$ template does not extrapolate to longer wavelengths in a linear way, and another level of detail must be added.

To good approximation, the error made by a linear model is a function only of ecliptic

latitude. Therefore, one must modulate the $25\mu\text{m}$ map by some reasonable function of ecliptic latitude. Rather than choose standard basis functions such as a series of ($m = 0$) spherical harmonics, SFD98 instead employs a function determined by the dust itself - simply the $25\mu\text{m}$ flux binned in ecliptic latitude. This modulation is adequate with only one term in the expansion, and comprises the so-called “quadratic zodiacal light model” (see SFD98, equation 3).

The success of such a method depends on a few assumptions. One is that the Galactic dust cirrus is negligible at $25\mu\text{m}$. SFD98 showed that, in any place where the $100\mu\text{m}$ flux is less than 100 MJy sr^{-1} , the $25\mu\text{m}$ flux due to cirrus causes at most a 1 percent error in the final map. Another assumption is that there is no CIB in the $25\mu\text{m}$ map. This approach will not be sensitive to any CIB component that has the same spectral shape as the zodiacal emission. Current models of the CIB predict no substantial flux at $25\mu\text{m}$, and certainly less than the flux at $140\mu\text{m}$ (in νI_ν units). If the CIB flux at $25\mu\text{m}$ were as high as it is at $140\mu\text{m}$ ($25 \text{ nW m}^{-2}\text{sr}^{-1}$), the offset introduced in the 60 and $100\mu\text{m}$ cirrus maps would be negligible ($3 \text{ nW m}^{-2}\text{sr}^{-1}$ at $60\mu\text{m}$ and $1 \text{ nW m}^{-2}\text{sr}^{-1}$ at $100\mu\text{m}$).

This “quadratic model” was used by SFD98 to separate cirrus (Galactic ISM) emission from CIB and zodiacal light. At 140 and $240\mu\text{m}$, the zodiacal emission is faint enough that its latitude dependence provides enough information to separate it from the CIB; at shorter wavelengths, more sophisticated methods are required.

2.1.2. *Goddard Zodiacal Emission Model*

The model invented by the Goddard team (Kelsall et al. 1998) is an ambitious attempt to parameterize the full spatial-temporal dependence of the IPD emission. It contains six components, a smooth cloud, circumsolar ring, a density enhancement following the Earth and in resonant lock, and also three dust bands near the ecliptic at 3 AU. Certainly, the complexity of the dust cloud justifies the 46 model parameters, and a sophisticated model is required to establish the isotropy of the background. However, even though the parameterization is physically well motivated, a simple subtraction of the model from the data leaves significant unexplained residuals at $\lambda \leq 100\mu\text{m}$. These residuals may result from detector gain drifts, or small variations in dust density and temperature. For this reason, a more robust approach is required.

The two methods given in §3 each construct a dimensionless parameter that is robust (at first order) with respect to gain drifts and dust density and temperature variation. This parameter is evaluated for each of the 40 weeks of the DIRBE mission, using the DIRBE

weekly skymaps with Galactic emission subtracted. Before discussing these methods in detail, we next consider the Galactic (ISM) emission removal from each weekly skymap.

2.2. Galactic ISM dust emission

Emission from Galactic dust in the ISM (cirrus) is typically comparable in brightness to the IR excess at $100\mu\text{m}$, and about $1/4$ as bright at $60\mu\text{m}$ (Fig. 1). As pointed out in the “zodiacal light” fits in SFD98, it is easier to separate the Galactic cirrus from the sum of the other emission components than it is to isolate the CIB. SFD98 describe FIR maps that have a “quadratic zodiacal light model” (actually zodiacal light plus CIB) removed, which we call the “cirrus-correlated maps.” These maps are constructed by removing a quadratic zodiacal emission model from the DIRBE annual average maps so as to maximize the correlation of the cirrus map with the Leiden-Dwingeloo H I survey at high galactic latitude (see SDF98 for details). Because only 3 degrees of freedom are used to fit the H I data to the full-sky DIRBE maps, the structure of the Galactic ISM is derived directly from the DIRBE maps, not from H I data. These annual-average DIRBE maps are subtracted from each weekly average DIRBE map before the processing described in §3 is performed. The structure of the Galactic cirrus and extragalactic point sources are therefore almost perfectly subtracted, with remaining residuals attributed to detector gain drift and shifted effective pixel centers from week to week.

The uncertainty in our final IR excess measurements resulting from the cirrus emission is discussed in §4.2. There may also be substantial emission from dust in the warm ionized medium (WIM), as traced by $\text{H}\alpha$ and pulsar dispersion measures. However, the WIM is well correlated with the CNM on spatial scales of interest, and this contribution should not result in a significant error. Section 4.2 gives a complete discussion of systematic uncertainty associated with the WIM dust.

The next section addresses the brightest foreground, the zodiacal light.

3. ZODIACAL EMISSION REMOVAL: TWO METHODS

3.1. Method I

Our first method makes use of the north-south variation of the zodiacal emission observed by DIRBE as a function of time. The Interplanetary Dust (IPD) cloud is inclined $\sim 2^\circ$ with respect to the ecliptic, resulting in a north-south asymmetry with a one year

period (see Figs. 2 and 3). At first, it appears that this temporal variation is an undesirable complication in an already complex problem. However, this temporal variation allows us to probe the dust cloud in the z direction (normal to the dust plane) and separate zodiacal emission from the other components. Because the temperature and density of the IPD change throughout the year, it is useful to consider a dimensionless parameter that corresponds to our z position in the IPD cloud, a number for which uncertainties in the overall IPD density and temperature cancel out. Therefore, it is convenient to define a dimensionless ratio,

$$R_b \equiv \frac{N_b - S_b}{N_b + S_b}, \quad (2)$$

where N_b (S_b) is the total DIRBE flux at the north (south) ecliptic pole in band b . In bands where the zodiacal light overwhelms emission from cirrus, CIB, or other contamination, this quantity is related only to the z position of Earth in the dust cloud - not to density or temperature. Because variations in dust temperature, density, and detector gain drifts cancel out in R_b , it is far more robust than any absolute measurements. In fact, R_b is nearly independent of IPD model. We are assuming that the z -dependence of IPD emission per volume has the same functional form for each waveband, which should be true for dust near the Earth. This requirement is not strictly satisfied by the IPD, but is justified in section 4.

Because it is exceedingly difficult to model the IPD cloud along all lines of sight at all times, we restrict ourselves to analysis of patches within 5° of the ecliptic poles. These regions contain data for every week of the DIRBE mission, and effects dependent on solar elongation angle cancel out to first order. We have prepared a mask for pixels in this region, excluding those pixels not present in symmetric combinations for each week. Details are given in §4.5.

Our resulting measurements of the IR excess at 60 and $100\mu\text{m}$ depend upon two main assumptions: (1) that the amplitude of the annual variation in R would be nearly constant in all wavebands in the absence of the excess, and (2) that our $100\mu\text{m}$ cirrus map (SFD98) is correctly zero-pointed. Both of these assumptions have been explored thoroughly, and are investigated in detail in §4.

Plots of R_{12} and R_{25} are shown in Figures 2b and 3b. The line is a simple sinusoidal model - the best fit for

$$R_{model} = A \sin(\nu - \nu_0) + C \quad (3)$$

where A is the amplitude, ν is the true anomaly (i.e. the angle, measured at the Sun, between perihelion and the Earth \approx true longitude minus 102.8°), ν_0 is a phase angle, and C is a small constant. The true anomaly, ν , is used instead of mean heliocentric longitude because it corresponds more directly to Earth's z position in the dust cloud. The deviations

between the model and data are too small to see in Figures 2 and 3, and therefore are plotted in Figure 4. The RMS dispersions of R_{12} and R_{25} relative to this simple model are 1% of the amplitude of the sine wave - and 0.1% of the total emission at the poles. Furthermore, there is a strong correlation between the residuals at 12 and 25 μm - suggesting that the residuals are physical. This is a powerful test of the relative photometric stability of the DIRBE 12 and 25 μm detectors, and allows us to proceed to the next step.

3.1.1. Scale-Height of the Dust

A common *Ansatz* for z -dependence of density in a disk is $\exp(-|z|/h)$ where z is the height above the dust plane and h is some scale height. Such a model has a density cusp at $z = 0$, but because we travel only $\sim 0.03\text{AU}$ in the z direction, the effect of the cusp is negligible. Another reasonable guess might be a gaussian

$$\rho = \rho_0 \exp(-z^2/2\sigma_z^2). \quad (4)$$

This distribution has the convenient property that $\rho(r, z)$ is smooth near $z = 0$, consistent with our sinusoidal fit. A third model is the Goddard widened fan model (Kelsall et al. 1998, Eq. [7]), with a vertical profile

$$f(\zeta) = \exp(-\beta g^\gamma) \quad (5)$$

where $\zeta \equiv |Z_c/R_c|$,

$$g = \begin{cases} \zeta^2/2\mu & \text{for } \zeta < \mu \\ \zeta - \mu/2 & \text{for } \zeta > \mu \end{cases} \quad (6)$$

and $\beta = 4.14 \pm 0.067$, $\gamma = 0.942 \pm 0.025$, and $\mu = 0.189 \pm 0.014$ are the best-fit values of the parameters.

Results presented in this paper are derived using the gaussian model and are indistinguishable from the other models. All we require is that the density distribution be reasonably smooth near $z = 0$ and not extend too high above the plane.

How much north-south variation is expected? Symmetry considerations suggest that the dust plane is approximately aligned with the invariable plane of the solar system, which is perpendicular to the total angular momentum vector of the solar system. The north pole of this plane is at $\alpha_{2000} = 273.85$, $\delta_{2000} = 66.99$ or $\lambda = 17.8$, $\beta = 88.42$ in ecliptic coordinates. (We denote the heliocentric mean ecliptic longitude of Earth with L hereafter in this paper, and reserve the usual symbol λ for wavelength.) This difference between the ecliptic plane and invariable plane is critical for our method, but the actual inclination

angle is nearly degenerate with the dust cloud height in our fits. Our results are the same whether the 1.58° angle to the invariable plane, or the 2.03° inclination of the Kelsall et al. 1998 smooth cloud is used.

The perihelion (minimum Earth-Sun distance) is at $L \approx 102.8^\circ$. The ascending node of the putative dust plane is at 107.8° . Because they are near each other, the time of maximal excursion from the dust midplane occurs when the Sun-Earth distance is approximately 1 AU. Therefore, the extreme values of z are ± 0.0276 AU. Within this range (according to the fit in Figure 3) resides $\sim 10.4\%$ of the dust. Simple algebra then gives a scale height of $\sigma_z = 0.20 \pm 0.01$ AU for the gaussian. This is very similar to the FWHM of the Kelsall model. Of course, the density profile need not be a gaussian in z ; if the emissivity of the IPD can be written as $I_b(z, r)n(z, r)$ then we have the model-independent constraint that

$$\int_{low}^{hi} I_b(z, r)n(z, r)dz = 0.104 \int_{-\infty}^{\infty} I_b(z, r)n(z, r)dz \quad (7)$$

We only use this to justify our assumption that the dust along a line of sight is near the Earth and of uniform temperature. None of the conclusions in this paper depend on the functional form of the z -dependence.

3.1.2. Model Fit

Now that we have established a reasonable model for the z dependence of dust emission, let us formalize it a bit. Suppressing the b subscript for convenience, let us define N (S) to be the total emission observed near the north (south) pole of the invariable plane:

$$N \equiv Z_N + B_N \quad (8)$$

$$S \equiv Z_S + B_S \quad (9)$$

where Z_N (Z_S) is the zodiacal light in the north (south) and B_N (B_S) is the time-independent background in the north (south), including cirrus, CIB, Reynold's Layer, and any other unknown backgrounds such as halo dust. Let us also define

$$Z \equiv Z_N + Z_S; B \equiv B_N + B_S \quad (10)$$

where Z is the total column emission through the IPD plane, while B is *twice* the average background.

For simplicity, we assume that the emission per volume is constant near the ecliptic plane, such that R depends only on $z = r \sin \theta \sin i$, with r and θ suitably defined for an

elliptical orbit. The position of Earth is parameterized by the true anomaly, ν , given in the almanac as (Astronomical Almanac 1991, p. E4):

$$\nu = M + (2e - e^3/4) \sin M + (5e^2/4) \sin 2M + (13e^3/12) \sin 3M + O(e^4) \quad (11)$$

where e is the eccentricity of Earth's orbit ($e \approx 0.0167$), $M = L - \tilde{\omega}$, L is the mean longitude and $\tilde{\omega} \approx 102.8^\circ$ is the mean longitude of perihelion. The true Earth-Sun distance is then

$$r = (1 - e^2)/(1 + e \cos \nu) \quad (12)$$

where r is in AU. We let Ω denote the nominal longitude of the ascending node of the dust plane (approximately $L = 77^\circ$) and define θ as

$$\theta = \nu + \tilde{\omega} - \Omega \quad (13)$$

The height of Earth above the dust plane is given by

$$z = r \sin \theta \sin i \quad (14)$$

where i is the inclination of the dust plane ($i \approx 1.58^\circ$). The zodiacal emission at the ecliptic poles is given by

$$Z_N = \frac{Z}{2} (1 + Ar \sin \theta) \quad (15)$$

$$Z_S = \frac{Z}{2} (1 - Ar \sin \theta) \quad (16)$$

and the ratio R by

$$R = A'r \sin \theta + C. \quad (17)$$

with the definitions

$$A' \equiv A \left(\frac{Z}{Z + B} \right); C \equiv \frac{B_N - B_S}{Z + B} \quad (18)$$

Here the constant factor $\sin i$ is absorbed in the A coefficient to emphasize that A and $\sin i$ are degenerate parameters in this model. The results of this paper do not depend on the value of $\sin i$ in detail, only that it be small and constant. Physically, A is the amplitude of the annual variation in R due to the zodiacal emission and A' is the observed amplitude.

The total background may now be expressed in terms of the observables, N and S :

$$B = (N + S) \left(1 - \frac{A'}{A} \right), \quad (19)$$

and the difference,

$$B_N - B_S = C(N + S), \quad (20)$$

which leads immediately to expressions for the north and south:

$$B_N = \frac{B + C(N + S)}{2} \quad (21)$$

$$B_S = \frac{B - C(N + S)}{2} \quad (22)$$

3.1.3. Results

Results of the fits in the DIRBE 5-240 μ m bands are presented in Table 1. The best-fit model parameters A' , ν_0 , and C are given for each waveband, as well as the derived parameters Z , B_N , and B_S . The value of ν_0 is determined from the 12 and 25 μ m bands and adopted for the others. Values of $A(\lambda)$ must be assumed in order to derive B from A' , and because the 25 μ m band is dominated by zodiacal emission, $A \approx A'$. As can be seen from the large errors for the 140 and 240 μ m bands, this method breaks down at long wavelengths where the zodiacal emission is weaker and the S/N of the detectors is much lower. Although the actual CIB level at 12 and 25 μ m is unknown, it must be non-negative. The assumption of a significant CIB in these wavebands would only increase the amount deduced for the longer wavelengths. Therefore, we assume the CIB at 25 μ m to be zero to make a conservative assessment of the emission at 60 – 240 μ m. The systematic errors introduced by this assumption are determined by computing the change in the measured excess if the 25 μ m CIB has the same νI_ν as 140 μ m. The large excess at 12 μ m is very uncertain, because of the larger model dependence at short wavelengths. The excess at 5 μ m is sufficiently model dependent that it should not be taken seriously.

Values for B_N and B_S are shown separately in Table 1 to demonstrate that the $N - S$ difference due to cirrus has been adequately removed from the weekly maps. We take the A dependence calculated for the Goddard widened-fan model, but consider other models in §4 to estimate systematic errors. This slight model dependence will propagate into our final systematic errors, but for now we retain the assumption that A is constant in every DIRBE band.

3.1.4. Model Refinements

The residual seen in Figure 4 suggests a residual with a 1/3 yr period at both 12 and 25 μ m. We have added a few parameters to the model to allow for two dust disks of different thicknesses, inclinations, and ascending nodes (similar to the “circumsolar ring”

in the Goddard model), and this improvement removes the 1/3 yr period signal. Another improvement was made to account for possible emission from interstellar dust grains focussed by the Sun into a cone in the downstream direction of the Sun’s motion relative to the local ISM. Although inclusion of these effects improves the χ^2 of the fit, the change is not substantial, and no significant variation in the derived IR excess results. They are therefore not considered further in this paper.

3.2. Method II

In this section, we present a method to disentangle the CIB from zodiacal emission by making use of the ecliptic latitude dependence of the latter. We define a dimensionless statistic, Ξ that can be measured independently for each of the 41 weeks of the DIRBE mission. This quantity is designed to be insensitive to the zodiacal emission model parameters. At the same time, this statistic provides a sensitive measure of any isotropic background. Although this statistic involves less robust assumptions about the IPD than method I, we test its dependence on the parameters of the Kelsall et al. (1998) model. The Ξ statistic allows for a wider range of statistical tests and addresses questions about isotropy. Furthermore, the assumption of a small CIB value at $25\mu\text{m}$ is not required.

In SFD98, the CIB was measured at $140\mu\text{m}$ and $240\mu\text{m}$ by fitting and removing a $\csc|\beta|$ slab component to the annual-average DIRBE skymaps at high Galactic latitude. Of course, the annual-average maps combine data from many solar elongation angles averaged over 41 weeks (not 1 yr) and contain the resulting artifacts. Moreover, there are theoretical and observational reasons to suspect that the IPD is a “modified fan” and not a slab at all (see Kelsall et al. 1998, §4.2 for discussion). In the limit where the zodiacal emission is small compared to the CIB, this method gives reasonable results, but fails badly at $\lambda \leq 100\mu\text{m}$. The basic idea can be used successfully, however.

By working only with solar elongation 90° data in each weekly map, the problem is conceptually simpler. In Figure 5 we show the volume emissivity density contours of the $e = 90^\circ$ plane, i.e., the plane containing Earth and perpendicular to the Earth-Sun line. The axes are labeled with Cartesian ecliptic coordinates, in AU. The Earth is in the middle (at a time of year when $x = 1, y = z = 0$), with lines of sight to the ecliptic poles labeled NP and SP, and the “forward” direction of Earth’s orbit to the right. Four other lines are drawn, all of which are at latitude $|\beta| = 45^\circ$. They are labeled NF for “North-Forward,” NB for “North-Backward” and so on. A convenient dimensionless ratio to define is:

$$\Xi(\beta) \equiv \frac{NF + NB + SF + SB}{2(NP + SP)} \quad (23)$$

This quantity is almost completely insensitive to vertical position in the dust cloud, to a small inclination of the dust cloud with respect to the ecliptic, dust temperature, or to nearly any other parameter in the Goddard (Kelsall et al. 1998) model. In fact, when $\Xi(\beta)$ is computed for the Goddard model (the most realistic model to date), its annual variation is negligible (< 0.001) for the latitudes of interest ($35^\circ < \beta < 50^\circ$).

If the zodiacal emission were approximately a slab, one would expect the functional dependence $\Xi(\beta) = \csc(\beta)$. It is notable, however, that the Ξ “measured” from the Goddard model at long wavelengths is significantly greater than $\csc|\beta|$ in the range of interest ($35^\circ < \beta < 50^\circ$). This is because the Rayleigh-Jeans emissivity density contours shown in Figure 5 (*solid contours*) follow the volume density contours closely, and the “fan” nature of the model causes an upward curvature of the contours, resulting in $\Xi(\beta) > \csc|\beta|$.

At short wavelengths, the situation is reversed. The emissivity is so temperature sensitive that distance from the Sun is the overriding concern. In this case, the emissivity contours curve downward, yielding $\Xi(\beta) < \csc|\beta|$ (Figure 5, *dashed contours*).

These deviations from the geometry of a uniform slab are fine points, and do not affect the measurements at 60 and 100 μm , as we shall see, but one must account for them carefully in order to measure the background at 3.5 – 12 μm , which is beyond the scope of the current paper.

For simplicity, we now return to the approximation that $\Xi_0 = \csc|\beta|$. Now let us consider the effect of an isotropic background, B , on observed values of Ξ .

$$\Xi = \frac{B + Z \csc|\beta|}{B + Z} = 1 + \frac{\csc|\beta| - Z}{B + Z} \quad (24)$$

where Z is $NP + SP$. Solving for B gives

$$B = \left(1 - \frac{\Xi - 1}{\csc|\beta| - 1}\right) I \quad (25)$$

where I is the observed flux at the poles ($Z + B$) and B is the twice the value of the CIB, as it was in method I. Figure 6 contains plots of Ξ at 35° for 60 and 100 μm applied to the cirrus-subtracted weekly DIRBE maps. . Unsurprisingly, the fit residuals are correlated from week to week. To account for this correlation, we estimate there are no more than 4 independent measurements within the 41 weeks, and thus the standard deviation of the mean of Ξ is reduced from the rms scatter by only $\sqrt{4}$.

Results for method II are shown in Table 2. For each latitude bin and each band b , Ξ_{K_b} is calculated from the Kelsall IPD model and compared with the measured Ξ_b .

The background, $B/2$, is then determined from eq. (25). A weighted average gives $28.0 \pm 1.9 \text{ nW m}^{-2}\text{sr}^{-1}$ at $60\mu\text{m}$ and $21.9 \pm 2.7 \text{ nW m}^{-2}\text{sr}^{-1}$ at $100\mu\text{m}$.

This agreement between the two methods is encouraging, and suggests that the observed excess is not coming from within the solar system, at least it does not vary spatially or temporally in the way the IPD is expected to.

4. SYSTEMATIC ERRORS

The DIRBE detector noise is small enough that measurement errors in the determination of the FIR excess are modest, but several distinct systematic errors contribute to the uncertainty in the final result. The IPD model dependence is discussed in §4.1 and possible emission correlated with the WIM is considered in §4.2. Section 4.3, more generally rules out emission from a dust slab aligned with the Galactic plane, and possible emission from the Galactic halo is addressed in §4.4. Final uncertainty estimates are presented in §4.5.

4.1. IPD Model Dependence

A fully self-consistent model of the IPD emission has not yet been found, probably because of the large number of dust components whose temperature and density may vary spatially and temporally. The Goddard model (Kelsall et al. 1998) is certainly the most complete, but it still must resort to fudge factors to explain the emissivity function of the IPD, and it assumes that the emissivities of the spatially separate components are identical. With currently available data, it is not economical to introduce still more parameters in order to solve this problem, so no CIB measurement that depends in detail on the zodiacal emission model can be trusted. However, the Kelsall et al. model is used as a reference model in the following.

Neither method described in the previous section is strongly influenced by this choice of IPD model. Our analyses rely only on data at high ecliptic latitudes, where many of the zodiacal components, such as the dust bands at $\beta < 15^\circ$ can be safely ignored. Furthermore, the dimensionless parameters, R and Ξ , can be predicted in a nearly model-independent way and readily compared with the data. The advantage of this approach is that the results depend on relative measurements made on short timescales, and are almost independent of the choice of IPD model. What little dependence there is enters the two methods in different ways.

4.1.1. Method I

For most reasonable models of zodiacal emission, the expected amplitude A in method I should be a weak function of wavelength, not a constant as we assumed. Figure 7a, shows the function $A(\lambda)$ predicted by the Goddard (Kelsall et al. 1998) model (*dot-dashed line*) compared to the observed $A'(\lambda)$ values. The solid line is the Goddard model evaluated at the poles of the dust plane instead of the ecliptic poles, for $T_0 = 286\text{K}$. In this model, the dust temperature depends on distance from the Sun, and T_0 is the temperature at 1 AU. The other lines are for T_0 higher and lower by a factor of two. Of course this is an absurdly large range of temperatures, but we use it to illustrate that for single emission components, the amplitude $A(\lambda)$ is nearly constant on the Rayleigh-Jeans side of the IPD spectrum. The dependence of A on other model parameters is similarly weak.

Two-component models of IPD can also be considered. If there are two distinct grain sizes with different T_0 , it is still impossible to fit the observations. In the worst-case scenario, the dust grains are segregated into two populations, one in a dust layer near the ecliptic plane, and the other away from it. The spectrum of A is then simply the ratio of the spectra of the two components - both of which have identical Rayleigh-Jeans tails.

In order to fit the observed $A'(\lambda)$ values with no background, one requires two populations of dust grains with different emissivity laws. An example of this is shown in Figure 7b - but this is an extreme case of grain properties and geometry constructed to give the desired result. In this model, the IPD away from the midplane is very similar to the Kelsall model: $T_0 = 286\text{ K}$, blackbody dust. However, the slice of dust within $|z| < 0.03\text{AU}$ (the extent of Earth's annual excursion from the midplane) has $T_0 = 236\text{ K}$ and $\nu^{0.5}$ emissivity. These parameters seem unlikely, but they greatly reduce the excess $60\mu\text{m}$ flux, and affect the $100\mu\text{m}$ excess slightly.

We considered a class of two-component models with different emissivity power laws, different temperatures, with one in a much thinner disk than the other. Exploring such models in detail, we found that it to be impossible to reduce the $60 - 100\mu\text{m}$ background substantially without either producing excessive emission in the $12\mu\text{m}$ zodiacal signal or going to unreasonable parts of the model parameter space.

We therefore proceed by assuming that an extrasolar, isotropic excess at $60\mu\text{m}$ is physically more acceptable than a contrived IPD emission model. The reasonable range of IPD models do not alter the derived 60 and $100\mu\text{m}$ excesses by more than $5\text{ nW m}^{-2}\text{sr}^{-1}$ (95% confidence).

4.1.2. Method II

Because method II is sensitive to the shape of the $e = 90^\circ$ emissivity contours (as seen in Fig. 5), it is immune to a two-component model of the type contrived above, as long as the components are layered with azimuthal symmetry. However, method II is in general more dependent upon the zodiacal light model used. This dependence is calculated by using the Kelsall et al. model as a reference IPD model. Table 3 displays the error in the IR excess measurements introduced by 1σ and 3σ changes in the main 6 parameters of the Kelsall model. Only the parameter α , (the density $\rho \sim R^{-\alpha}$) affects method II results significantly. This is not surprising, because α affects the shape of the IPD cloud more than most of the other parameters. Uncertainties in the Kelsall model propagate into our results only at the level of $3 \text{ nW m}^{-2}\text{sr}^{-1}$ at $60\mu\text{m}$ and $1 \text{ nW m}^{-2}\text{sr}^{-1}$ at $100\mu\text{m}$ (95% confidence). If the Kelsall model provides a reasonable description of the shape of the IPD cloud, then the model uncertainties cannot be much bigger than this. If, however, the Kelsall model is missing a substantial component that changes the emissivity contours' shape in the $e = 90^\circ$ plane, then the uncertainty could be much larger.

4.2. Dust Emission from the ISM

In this section we assess the uncertainty in the IR excess described above due to a zero-point error in the Galactic ISM (or cirrus) emission maps. According to SFD98, Table 2, the largest formal uncertainty in the cirrus emission is less than $1 \text{ nW m}^{-2}\text{sr}^{-1}$. However, there is a larger systematic uncertainty resulting from neglect of dust in the warm ionized medium (WIM). The issue is not whether there is dust in the WIM; all ISM dust emission, described by the SFD98 cirrus maps, is subtracted from the DIRBE weekly maps before R and Ξ values are fit. However, any zero point error in the SFD maps will propagate directly into the measurement of the CIB. In fact, the flux measured at the poles contains no cirrus and are essentially a full-sky zodiacal light fit, evaluated at the poles (method I) and at other latitudes (method II). This is important for isotropy considerations, because the results we obtain effectively use data from the entire high-latitude sky via the SFD98 fit to the Leiden-Dwingeloo H I survey.

4.2.1. Correlation with H-alpha

One tracer of the WIM that can be used to constrain the cirrus zero-point is H α emission. A recent paper by Lagache et al. (1999) addresses this question. Using the

high-quality H α data of Reynolds et al. (WHAM; Haffner et al. 1998) to trace the WIM, they claim to find significant WIM emission at 100 – 1000 μ m, using 2% of the sky at high galactic and ecliptic latitude, and H α emission between 0.2 and 2 R. We have repeated their analysis with the same data in the same regions of the sky and find no WIM dust emission uncorrelated with H I emission. This high-latitude analysis provides no indication that our zero-point is incorrect.

Although we are interested in zero point problems in the diffuse cirrus at high galactic latitude, where the SFD98 zero point was determined, we must resort to a different analysis that makes use of H α data closer to the galactic plane where the signal is strong. This will provide a “worst case” result. Heiles et al. have shown that a simultaneous fit of H I and H α yields only a modest shift in zero point (Heiles, Haffner, & Reynolds 1999). In several regions near Eridanus, they perform a fit of the form

$$I_\lambda = A + BN(\text{HI}) + CN(\text{H}\alpha) \quad (26)$$

and find that A varies by approximately 6 nW m⁻²sr⁻¹ RMS at 100 μ m in the various regions, with a central value of 2 nW m⁻²sr⁻¹. These fits are performed with the SFD98 100 μ m map which already has a model of zodiacal light+CIB removed, i.e., it is zeroed to H I. The fact that these offsets are so near zero indicates that the dust correlated with H α might possibly explain as much as 6 nW m⁻²sr⁻¹ (the extreme case found by Heiles et al.) of our ~ 30 nW m⁻²sr⁻¹ background measurement at 100 μ m, but is not likely to significantly alter the result.

Although the H α result is encouraging, it suffers from a few weaknesses. The sky coverage is small (2% in Lagache et al. $\sim 10\%$ in Heiles et al.), and future analyses using the entire WHAM data set may provide more concrete answers. Also, the H α emission is not proportional to N(H II) but rather to $\int n_p^2 dl$ and is also weakly dependent on temperature. This means that a correlation of H II density and dust/gas ratio could contrive to produce $A \approx 0$ even though the derived zero point is incorrect. Therefore, an alternative method is desirable as a confidence check.

4.2.2. Pulsar Dispersion Measures

The pulsar dispersion measure is a straightforward determination of the column density of electrons $N(e^-)$ along the line of sight to a pulsar. It does not depend on the temperature or density of the ionized gas, but does rely on the pulsar being far enough away to give a fair assessment of the Galactic H II. For this work, we have made use of the pulsar catalogue

assembled by J. Taylor at Princeton (Taylor et al. 1993 ¹).

The catalogue contains 707 pulsars, 146 of which are at $|b| > 20^\circ$ and have distance quality codes of “a” or “b”. Of these, 108 are in the region covered by the Leiden-Dwingeloo survey, allowing a comparison of $N(e^-)$ and H I with $100\mu\text{m}$ flux. A further requirement that the pulsars be out of the plane ($|z| > 400\text{pc}$) reduces the list to 46. As one can see in Figure 8, the zero point of the H/dust regression changes only modestly when the pulsar data are included, even though the slope changes by roughly 1/3. This indicates that H I and H II are correlated, but perhaps are no more correlated than any other $\sim \csc |b|$ mechanism. Because the scatter is no tighter with H II included, one might conclude that there is little dust associated with H II. On the other hand, the poor assumption that each pulsar is behind all Galactic dust may add noise, cancelling out the improvement.

Curiously, the y -intercept in 8(a) is not zero, even though it is forced to be (by construction) over the average high-latitude sky (see SFD98). This nonzero intercept may indicate variation in the gas/dust ratio - even at high $|b|$, or may also reflect large-scale gradients in the SFD98 dust model. Whether the SFD98 temperature correction is used or not, we find that the largest zero-offset induced by such changes is at most 0.1 MJy sr^{-1} ($3 \text{ nW m}^{-2}\text{sr}^{-1}$) at $100\mu\text{m}$. If we assume that perhaps half of the dust emission emanates from above the 400pc pulsar cut, and double this effect, it is still negligible. Furthermore, if we consider the change in zero point due to the use of a temperature correction as a systematic error that propagates directly to the IR excess, we still find a systematic uncertainty of only $6 \text{ nW m}^{-2}\text{sr}^{-1}$. Because this is an uncertainty similar to that obtained from the H α analysis of Heiles above, we adopt $6 \text{ nW m}^{-2}\text{sr}^{-1}$ as the (95% conf.) uncertainty associated WIM-correlated dust emission, and add this to our systematic error budget (Table 4) at 60 and $100\mu\text{m}$.

4.3. Ruling out a dust slab

There is still a chance that a diffuse layer of dust more than 400pc above the disk of the Galaxy could be responsible for the emission. Such a layer, if behind most of the pulsars, could be either uncorrelated with H α emission, or could be associated with H II so diffuse that H α emission is effectively suppressed. This sort of a foreground would be indistinguishable from the IR excess using the methods described in this paper, but would reveal itself by a dependence on Galactic latitude.

¹The latest version is available at <http://pulsar.princeton.edu/ftp/pub/catalog/>.

Because the DIRBE data do not extend over a full year, and because of drifts in the zodiacal light intensity and detector gain with time, the annual average maps contain unphysical gradients that may confuse a direct fit of a $\csc |b|$ component. In order to test for the presence of such a component, we again introduce a dimensionless parameter.

For each weekly DIRBE map, we construct a dimensionless parameter χ from the flux in four patches on the sky, always placed at solar elongation $|e| = 90^\circ$ and $|\beta| = 75^\circ$.

The mean flux values in the four patches of sky are designated I_{NF} for “North-Forward”, I_{NB} for “North-Backward”, and likewise I_{SF} , and I_{SB} for the south, just as in the definition of Ξ . In this case, “North forward” refers to a direction on the sky $(\lambda, \beta) = (L_{true} + 90, +75)$ where L_{true} is the true heliocentric longitude of Earth. The $L_{true} + 90$ direction does not correspond precisely to the direction of Earth’s velocity around the Sun because of eccentricity; rather it is at solar elongation 90° . These values are computed for each week of data, except when any of the patches is at low Galactic latitude ($|b| < 10^\circ$)

The four lines of sight used each week form an “X” in space. Two useful combinations are $I_A = I_{NF} + I_{SB}$ and $I_B = I_{NB} + I_{SF}$. We then define the dimensionless ratio

$$\chi = \frac{I_A - I_B}{I_A + I_B} \quad (27)$$

in which gain drifts and dust variations nearly cancel out. Because I_A and I_B are measured at solar elongation 90° , χ would be zero in the absence of ISM emission, if the IPD were aligned with the ecliptic plane. Misalignment with the ecliptic plane will produce a periodic signal in χ , revealing the inclination of the dust plane if the ascending node is known. Likewise, a uniform slab of emitting material will contribute another $\csc |b|$ periodic term. Unfortunately, the Galactic plane and dust midplane have similar ascending nodes so that their signal in this statistic is nearly degenerate, making a simultaneous fit impossible. Fortunately, an error of 1° in the inclination of the dust plane would result in an error of 1.5 and 0.3 nW m⁻²sr⁻¹ at the poles in the 60 and 100 μ m channels respectively. An isotropic background does not contribute to χ .

As an example of the power of this technique, we display in Figure 9 χ_{60} and χ_{100} for the 60 and 100 μ m channels after removal of the H I correlated component. For these fits, we used the inclination angle $i = 2.03^\circ$ obtained by the DIRBE team (Kelsall et al. 1998). Before H I removal (not shown in figure) the $\csc |b|$ term is strong, with values of 40 and 100 nW m⁻²sr⁻¹ at the Galactic poles for 60 and 100 μ m respectively. The flux is twice that at the ecliptic poles at $|b| = 29.8^\circ$. After removal of the best fit H I coefficient, only a small signal is left, at the level of 2.5 and 1.2 nW m⁻²sr⁻¹. Even though we have not explicitly removed a $\csc |b|$ component, the H I fit appears to have done so. The same procedure is difficult in the other wavebands. The noisy 140 and 240 μ m channels do not

give a meaningful measurement of χ , and at 12 and $25\mu\text{m}$ the technique is much more sensitive to the inclination angle of the dust plane.

This small residual signal at 60 and $100\mu\text{m}$ may reflect a small error in the H I subtraction, or may actually be an emission component not correlated with H I . Whether real or not, this component is very small compared to the IR excess measured in this paper, and in fact is small compared to the WIM error derived above. Therefore, we consider the error due to a Galactic slab to be already included in the WIM error adopted above.

4.4. Galactic Halo Dust

In this section we consider another potential component of Galactic emission which would not have appeared in this other tests: dust emission in the halo of our galaxy. We have ruled out dust correlated with $\text{H}\alpha$, dust correlated with H II within 400pc of the Galactic plane, and dust in a roughly $\csc |b|$ distribution. However, a very diffuse component of dust mixed into the Galactic halo – associated with ionized H or perhaps no gas at all – has not been strictly ruled out. The marginal detection of reddening along lines of sight passing near spiral galaxies (Zaritsky 1994) implies that there may be dust at $r > 60\text{kpc}$, although it is another question whether such dust is warm enough to mimic the measured excess. Alton et al. (1998) have observed cold (15K) dust 2 kpc off the disk of NGC 891 with SCUBA, but such dust would not give the observed signal at 60 and $100\mu\text{m}$ (see also Howk 1999).

Mechanisms that transport dust from the Galactic disk into the halo by radiation pressure have been proposed (e.g. Ferrara et al. 1991), but contain only crude approximations to the Galactic magnetic field. Consideration of a more realistic magnetic field would increase the diffusion time and increase the probability of dust destruction. The dust which makes it into the halo, if any, might be expected to be hotter than the disk dust, as long as the radiation field is similar. The grains should be smaller, and thus attain a higher equilibrium temperature; and the radiation pressure mechanism preferentially transports grains with a high optical/UV cross section to mass ratio - and these may also tend to be hotter. However, to explain the observed spectrum, they must be quite hot. Taking the warm $\nu^{2.6}$ component from Finkbeiner et al. (1999), a temperature of ~ 28 K must be maintained to explain the observed spectrum - in contrast to an average interstellar dust temperature of 18 K for single-component ν^2 models or 16 K for the warm component of the Finkbeiner et al. two-component model.

Such a halo must also be nearly isotropic. The halo proposed by Ferrara et al. (Fig. 2

in Ferrara et al. 1991) is unlikely, as it would have been detected by the method described in §4.3. In fact, a uniform spherical dust halo bright enough to explain the IR excess would appear isotropic enough for $r_{halo} \gtrsim 20\text{kpc}$ that it would not be noticed in any conceivable analysis of the DIRBE data. The theoretical complications of such a halo are many, but are perhaps no more distasteful than the conflict this IR background causes with TeV gamma ray observation, as we discuss in §5.2. However, the idea appears to be ruled out by the observational non-detection of a $60\mu\text{m}$ halo in M31 at the level of $\sim 0.1 \text{ MJy sr}^{-1}$ ($5 \text{ nW m}^{-2}\text{sr}^{-1}$). In fact, Rice et al. (1988) found no evidence that the IRAS $60\mu\text{m}$ emission of optically large galaxies extends into the halos. It is difficult to see why our Galaxy should be any different.

To summarize this section, if there is indeed a component of dust in our Galaxy that accounts for the IR excess, it must be uncorrelated with $\text{H}\alpha$, more than 400pc off the plane, and differ substantially from $\text{csc } |b|$. This forces us to seriously consider the possibility that the observed excess is mostly extragalactic in origin.

4.5. Final Results

In this section, we average the results from methods I and II and state the final results for the DIRBE 60 and $100\mu\text{m}$ channels, including systematic uncertainties. The casual reader should skip directly to §4.5.3

4.5.1. Method I

In method I, several computational choices introduce systematic uncertainties. One choice is whether to take a mean, median, or mid-average of the pixels at the ecliptic poles in each week. Some outlier rejection is necessary because of imperfect point source removal. However, because there is a gradient across the polar cap (due to solar elongation dependence) a mean is more stable. All results in this paper were derived with a mid-average, in which the highest and lowest 10% of the values are discarded, and the remaining values averaged. This proves to be more robust than either a mean or a median. Use of a mean increases our results by $\sim 5 \text{ nW m}^{-2}\text{sr}^{-1}$ at $60\mu\text{m}$ and twice that at $100\mu\text{m}$. However, a straight mean also results in an unacceptable $N - S$ asymmetry (formally 25σ at $25\mu\text{m}$) which is not present when a mid-average is used.

Another choice is the size of the polar region. Ecliptic latitude cuts of $|\beta| = 85^\circ$ and $|\beta| = 87^\circ$ were tested. The 85° cut provides adequate signal, but excludes the brightest

parts of the LMC. The variation introduced by this choice is negligible at 60 and 100 μm , but large at 140 and 240 μm . This is because the uncertainty in those channels is dominated by measurement noise, and a $|\beta| = 87^\circ$ leaves much less signal to work with.

The use of the ecliptic pole is motivated by the obvious symmetries. Another potential choice is the apparent pole of the dust plane, which is inclined $\sim 2^\circ$ with respect to the ecliptic. This choice can modify results by 5 nW m $^{-2}$ sr $^{-1}$.

A number of pixels are discarded for lack of coverage. Some weeks of DIRBE data, particularly “science” weeks 20 and 35 (numbered 0 to 40) contain very little sky coverage and are rejected. Other weeks with more than 10% bad pixels at the poles are also discarded so as not to mask out too many pixels in the remaining weeks.

The masks are generated independently for each waveband, which may raise questions about comparing the derived A' and C parameters for each waveband. However, the amplitude A determined at 12, 25 μm is quite insensitive to the mask used. One can take the union of multiple masks and apply that “master” mask to each waveband and still obtain the same results, though with lower signal-to-noise. We have no indication that such a procedure is necessary, so we simply apply to each waveband its own mask. Table 5 shows the fraction of pixels lost due to the mask in each waveband, and the number of weeks of good data used.

Even the method of pixel mask symmetrization calls for some judgment. For each bad pixel (λ, β) , it is necessary to mask $(\lambda, -\beta)$, or else the solar elongation gradient will be aliased into the time domain, and appear as signal in R . In fact, masking $(-\lambda, -\beta)$ and $(-\lambda, \beta)$ corrects this problem to a higher order. This 4-fold mask symmetrization was followed for all Method I results. Failure to symmetrize the mask in this way adds 2 nW m $^{-2}$ sr $^{-1}$ at 60 μm and 6 nW m $^{-2}$ sr $^{-1}$ at 100 μm .

In light of these systematic errors, we assign a systematic uncertainty of 7 (11) nW m $^{-2}$ sr $^{-1}$ at 60 (100) μm to method I (95% conf.), in addition to the formal statistical errors. At 140 and 240 μm , measurement noise dominates, so no such systematic errors are added.

The intent of method I is to make reliable IR excess measurements at 60 – 240 μm , but the less reliable results obtained at shorter wavelengths are interesting as well.

The flux measured at 12 μm ($\sim 2\%$ of zodiacal light) is almost certainly an artifact of the greater model dependence at short wavelengths. The 5 μm emission shown in Table 1 is relatively stronger ($\sim 10\%$ of zodiacal light) but is subject to extreme model dependence. It is interesting that this flux level of ~ 23 nW m $^{-2}$ sr $^{-1}$ is similar to the 5 μm excess found

by Dwek & Arendt (1998). They declined to call this a CIB because of anisotropy. This agreement between the two numbers may only be a curious coincidence.

4.5.2. Method II

In method II, there are fewer choices to make. Each line of sight uses pixels in a 5° diameter patch, as this is the largest patch that will be statistically independent from week to week and latitude bin to latitude bin. This method is sufficiently robust that the choice of the ecliptic as the symmetry plane is unproblematic: the Kelsall model gives less than 1 part in 1000 variation in Ξ due to this choice. In fact, the only significant systematic error this method has in common with method I is the mask-symmetry error, which we take to be the same as in method I. We therefore adopt a systematic uncertainty of 2 (6) nW m⁻²sr⁻¹ at 60 (100) μ m for method II.

4.5.3. Combined Results

The two methods are complementary: the first uses time-variability at the ecliptic poles for the analysis, and the second uses the spatial morphology of the data in each week. Method II is superior in that it samples a larger fraction of the data set and achieves a much higher S/N, but the use of different regions of the sky in each week results in systematic errors that are difficult to understand in detail. Therefore, there is no *a priori* reason to prefer one method over the other. We combine the results with a weighted average, using the formal random errors and systematic errors that apply to each method. Such errors average down when results of the two methods are combined (see Table 4). The remaining systematic errors that apply to *both* methods, such as the uncertainty in the ISM emission, are added after this averaging.

In Table 6 the results for method I, method II, and the average are stated. These numbers represent the FIR excess in 60 and 100 μ m DIRBE filters, which are calibrated assuming a flat spectrum in νI_ν . Color corrections for plausible FIR background spectra do not change these results by more than 10 – 20% (see DIRBE Exp. Supp. 1995).

5. DISCUSSION

Because we are unable to find any emission component within the Galaxy to explain the observed IR excess, we tentatively interpret the emission as an isotropic extragalactic

background (CIB). In this section we discuss the consequences of such an interpretation.

5.1. The EBL Energy Crisis

The integrated energy in the CIB for $60\mu\text{m} < \lambda < 1\text{mm}$ is $40 \pm 12 \text{ nW m}^{-2}\text{sr}^{-1}$ according to our measurements and those of Fixsen et al. (1998) - roughly twice the FIR energy content inferred from Hauser et al. (1998), and much higher than that predicted by Malkan & Stecker (1998). Where is this energy coming from? A comprehensive analysis by Bond, Carr, & Hogan (1986) reviews several possible sources for the FIR background, including primeval galaxies, pregalactic stars, black hole accretion, and decaying particles. Nuclear fusion within stars at epoch z contributes a radiation energy density Ω_R today (in units of the critical density) of

$$\Omega_R \approx 0.007 \frac{\Delta Z}{1+z} \Omega_B \mathcal{F} \quad (28)$$

where Ω_B is the baryon density of the Universe today (e.g. $\Omega_B h^2 = 0.019 \pm 0.001$; Burles & Tytler 1998), ΔZ is the mean metallicity of *all* baryons in the Universe, and \mathcal{F} is the fraction of the emitted radiation which is reprocessed into the FIR.

Black hole accretion is another source of energy for the CIB and yields a radiation density

$$\Omega_R = \left(\frac{\epsilon}{1-\epsilon} \right) (1+z)^{-1} \Omega_{BH,acc} \mathcal{F} \quad (29)$$

where $\epsilon \approx 0.1$ is the efficiency of rest mass to energy conversion and $\Omega_{BH,acc}$ is the mass density of accreting black holes.

With the definition of the critical density, $\rho_{crit} = 1.9 \times 10^{-29} h^2 \text{g cm}^{-3}$ and $h = H_0 / (100 \text{ km s}^{-1} \text{ Mpc}^{-1})$, the detected background of $40 \text{ nW m}^{-2}\text{sr}^{-1}$ becomes $\Omega_{CIB} = 9.8 \times 10^{-7} h^{-2}$. If this radiation was generated within stars and mostly reprocessed into the FIR at $z \approx 2$, then $\Delta Z \approx .02$, (regardless of h) averaged over the entire Universe. This seems rather large, and would indicate that most star formation must be well hidden from view.

Another possibility is generation of the CIB by accretion onto black holes, again at $z \approx 2$, with most of the radiation emerging in the FIR. If the black holes were formed by the accretion of baryonic matter ($\Omega \approx 0.019 h^{-2}$), with an efficiency $\epsilon = 0.1$, then the cosmological density of black holes today must be $\Omega_{BH} \approx 2.9 \times 10^{-5} h^{-2}$ and the fraction of all baryons that must have fallen into massive black holes (assuming no accretion of dark matter) is approximately 0.15%. While this number is large, it is smaller than the black hole mass fraction of 0.5% in galactic bulges (Magorrian et al. 1998).

It is also possible that energy extraction from black hole accretion is more efficient than assumed above. Recent work by Gammie (1999) indicates that for rotating black holes with a magnetic field, accretion efficiencies of $\epsilon \approx 0.5$ are possible. This reduces the requirement to 0.015% of baryon mass in black holes, consistent with the Magorrian et al. measurement and a disk/bulge mass ratio of ~ 30 .

Recent work (Almaini et al. 1999) shows that AGN observed by Beppo-Sax can explain the 30 keV X-ray background, and concludes that most of the energy generation takes place in obscured AGN. However, those AGN have only been shown to contribute 10-20% of the extragalactic background at 240 and 850 μm , and are unlikely to produce the measured flux at 60-100 μm . A recent model by Fabian (1999) suggests that the majority of black holes undergo a highly obscured growth phase, and predicts a population of objects at $z > 1$ which emit predominantly hard ($E > 30$ keV) X-rays and FIR/submillimeter photons. The Chandra telescope has recently resolved the majority of the 2-10 keV background, finding two new classes of objects: 1) optically “faint” galaxies ($I \gg 23$) with very high X-ray to optical ratios, and 2) point-like, luminous hard X-ray sources in the nuclei of normal bright galaxies showing no other sign of activity (Mushotzky et al. 2000). The former group is consistent with either early quasars, or extremely dust enshrouded AGN at $z > 2$. Conceivably some combination of accretion onto black holes and powerful starbursts within the core regions of merging galaxies is capable of explaining the IR excess reported here.

The spectral shape of the IR excess also has interesting implications. Because the 60/100 μm ratio is ~ 1 (in νI_ν units) the source must have a high dust temperature of $T \approx (1+z)28$ K. For $z \approx 2-3$ this temperature indicates a violent process is at work, and argues in favor of a few hot, bright sources. SIRTf will provide valuable information about the luminosity function of such sources at 24, 70, and 160 μm .

5.2. TeV Gamma Crisis

Another observational conflict is inevitable if the observed IR excess is of extragalactic origin: the observation of gamma rays by HEGRA (Konopelko et al. 1999, Aharonian et al. 1999) at energies up to $E \approx 20$ TeV from Mkn 501, and by Whipple (Samuelson et al. 1998) up to $E \approx 10$ TeV. The γ -ray opacity on CIB photons may be approximated by

$$\tau_{\gamma\gamma}(E_\gamma) \approx 0.24 \left(\frac{E_\gamma}{1 \text{ TeV}} \right) \left(\frac{u(\epsilon_*)}{10^{-3} \text{ eV cm}^{-3}} \right) (z_S/0.1) h_{60}^{-1} \quad (30)$$

where $u(\epsilon_*) = \epsilon_*^2 n(\epsilon_*)$ is the typical energy density in an energy band centered on ϵ , h_{60} is the Hubble constant, and z_s is the source redshift (see Coppi & Aharonian 1999).

Integrating the exact cross section over the DEBRA (Diffuse Extragalactic Background Radiation, including CMBR, CIB and optical/UV EBL), Stecker & de Jager (1998) find an optical depth of 2.5 at 20 TeV photons using a CIB prediction (Malkan & Stecker 1998) based on an extrapolation of *IRAS* counts and other data. The HEGRA data are consistent with this value at 20 TeV (Konopelko et al. 1999). However, using the currently accepted measurements of the CIB, Coppi & Aharonian (1999) obtain an optical depth $\tau \approx 5$ for 20 TeV photons. If we modify the CIB spectrum to take account of the 60-100 μm CIB measurements given in this paper, τ doubles to ~ 10 . Even without this doubling, the TeV observations imply that the intrinsic Mkn 501 spectrum is concave upward in the 10-30 TeV range, contradicting the synchrotron self-Compton emission model which requires it to be concave downward. Including the current CIB measurements would imply the intrinsic Mkn 501 spectrum increases a factor of 1000 in νF_ν from 10 to 20 TeV. Although very little is yet known about the true intrinsic spectrum of these blazars, this seems an unlikely explanation (however, see Mannheim 1999 for an alternative emission model).

There has also been speculation (Harwit, Protheroe, & Biermann 1999) that multiple TeV photons may be emitted coherently by blazars such as Mkn 501, and might arrive in Earth's atmosphere so close in time and space that they are confused with a single-photon event. Such coherent emission seems implausible, given the very large phase space available to TeV photons, but some similar mechanism might yet resolve the apparent conflict between TeV gamma observations and the expected opacity of the CIB.

Still more radical explanations have been proposed. Coleman & Glashow (1997, 1999) have proposed that quantum gravity effects cause a small violation of the invariance principle for very high energy particles. This effect may be large at the Planck scale (10^{19} GeV) but even at 20 TeV could have measurable consequences. Kifune (1999) has shown that one possible effect of such a violation is a sudden drop in the effective γ -ray / IR cross section for $E > 10$ TeV. The resulting dispersion relation may also have observable consequences for γ -ray bursts at cosmological distances (Amelino-Camelia 1998). Future TeV γ -ray data may rule out these quantum gravity theories, or perhaps demand a further exploration.

5.3. Future Data

Data to be gathered within the next few years should be adequate to resolve the problems discussed in this paper. The Space Infra-Red Telescope Facility (SIRTF) will obtain deep number counts at 25, 70, and 160 μm with the Multiband Imaging Photometer (MIPS) (Rieke et al. 1996). If the integrated flux from measured sources sums to the

observed IR excess, then the TeV γ -ray measurements must be reinterpreted. However, if the source density of objects generating the CIB is sufficiently high, then the deep SIRTf images will be confusion limited, and constraints on this diffuse emission will have to come from a fluctuation analysis, in which separation of the extragalactic component from the diffuse cirrus emission of our galaxy will be a limiting factor. Non-detection by SIRTf would confine the emission to our Galaxy, indicating either Galactic halo dust emission, a serious systematic calibration problem in the COBE/DIRBE instrument, a new emission component, or a serious flaw in the present analysis.

Another test is to observe more blazars at still higher energies. By combining data from blazars at different distances and different energies, one can place reliable limits on the DEBRA intensity, as long as the intrinsic blazar spectra are at all similar, or can be predicted by their relation to the X-ray emission from these objects. Work by the HEGRA and Whipple collaborations is underway.

6. SUMMARY

Previous attempts by the DIRBE team to measure the cosmic IR background made use of a sophisticated model of the Inter-Planetary Dust (IPD) (Kelsall et al. 1998). Such detailed modeling was necessary to establish the isotropy of the CIB signal detected at 140 and 240 μ m. The DIRBE team found excess emission at 100 μ m also, but doubted the isotropy of the emission and declined to call it a measurement. In order to recover the valuable information about galaxy formation and evolution contained in the CIB, we have measured the FIR excess at 60 and 100 μ m.

We analyze the excess DIRBE emission using two different methods. Each of these methods uses a dimensionless parameter derived from the DIRBE data in each week of the mission, parameters that are robust with respect to dust temperature and density variation and detector gain drift. These statistics are nearly insensitive to details of the IPD model. It is not necessary to know the IPD emission for every line of sight at every time, although we use the Kelsall et al. (1998) model as a reference. Method I uses time variation observed in the flux at the ecliptic poles to measure the background at the poles. Method II uses the spatial “shape” of the $e = 90^\circ$ data for each week to remove it and yields an independent measurement of the background in each week. Results derived from these two methods are consistent with each other, giving a background of $\nu I_\nu = 28.1 \pm 1.8 \pm 7$ nW m⁻²sr⁻¹ at 60 μ m and $24.6 \pm 2.5 \pm 8$ nW m⁻²sr⁻¹ at 100 μ m.

A variety of arguments rule out alternative sources of emission. Analyses of pulsar

dispersion measures and WHAM H α data demonstrate that signal from the WIM-correlated dust is already accounted for in the cirrus zero point determined from H I. After removing the cirrus, there is no additional component of this emission correlated with $\csc |b|$, arguing against any additional dust slab aligned with the Galaxy. The absence of extended far-IR emission halos around nearby galaxies (e.g. M31) rules out dust emission from extended halos. Unable to find an alternative emission mechanism, we cautiously consider the implications if this excess is an extragalactic background.

The energy required to produce a 44 ± 9 nW m $^{-2}$ sr $^{-1}$ integrated FIR background is large compared to the energy expected from stellar fusion. If the observed flux is indeed of extragalactic origin, then stellar fusion is probably not the dominant source of energy in the universe. Alternative sources such as highly obscured AGN at moderate redshift are a possibility, but would predict that 0.15% of all baryons are in black holes at the present time (although this figure is uncertain by a factor of ~ 10 because of uncertainty in accretion efficiency). A large X-ray background would also be predicted, unless the obscuration is of sufficient optical depth ($N(H) > 10^{24}$) to block it. The most serious problem with an extragalactic origin of the IR excess is the observation of TeV gamma rays. The opacity of the measured CIB to 20 TeV photons coming from Mkn 501 is 10 optical depths, much greater than the apparent absorption measured by HEGRA (see §5.2). Because of these inconsistencies, there is currently no satisfactory explanation for the observed excess, especially at 60 μ m. We continue to search for possible sources of emission in the solar system or Galaxy that could account for the observed emission, and urge caution in the use of these results. We eagerly await source counts from SIRTf and the X-ray observatories that might help to solve this mystery.

7. ACKNOWLEDGMENTS

We would like to thank Carl Heiles, Chris McKee, Bill Reach, Rick Arendt, and Eli Dwek for helpful discussions. Computers were partially provided by a Sun AEGP Grant. DJS is partially supported by the *MAP* project and by the Sloan Digital Sky Survey. This work was supported in part by NASA grants NAG 5-1360 and NAG 5-7833. The *COBE* datasets were developed by the NASA Goddard Space Flight Center under the guidance of the *COBE* Science Working Group and were provided by the NSSDC.

REFERENCES

Aharonian, F. A. & the HEGRA collaboration 1999, A&A, 349, 11

- Almaini, O., Lawrence, A., & Boyle, B. J. 1999, MNRAS, 305, L59
- Altieri, B. et al. 1999, A&A, 343, L65
- Alton, P. B., Bianchi, S., Rand, R. J., Xilouris, E. M., Davies, J. I., & Trewhella, M. 1998, ApJ, 507, L125
- Amelino-Camelia, G., Ellis, J., Mavromatos, N. E., Nanopoulos, D. V., & Sarkar, S. 1998, Nature, 393, 763
- The Astronomical Almanac 1991, (Washington, D.C.: U.S. Government Printing Office)
- Barger, A. J. et al. 1998, Nature, 394, 248
- IRAS Catalogs and Atlases: Explanatory Supplement 1988, eds. Beichman, C. A., Neugebauer, G., Habing, H. J., Clegg, P. E., & Chester, T. J. (Washington, D.C.: U.S. Government Printing Office)
- Bernstein, R. A. 1997, PhD Thesis, California Institute of Technology
- Blain, A. W., Jameson, Allon, Smail, Ian, Longair, M. S., Kneib, J.-P. & Ivison, R. J. 1999, MNRAS, 309, 715
- Blain, A. W., Kneib, J. P., Ivison, R. J., & Smail, I. 1999, ApJ, 512, L87
- Bond, J. R., Carr, B. J., & Hogan, C. J. 1986, ApJ, 306, 428
- Burles, S., Tytler, D. 1998, ApJ, 507, 732
- Coleman, S., & Glashow, S. L. 1997, Phys. Lett. B, 405, 249
- Coleman, S., & Glashow, S. L. 1999, hep-ph/9812418
- Coppi, P. S., & Aharonian, F. A. 1999, astro-ph/9903160
- COBE* Diffuse Infrared Background Experiment (DIRBE) Explanatory Supplement, ed. M. G. Hauser, T. Kelsall, D. Leisawitz, & Weiland, J. 1995, *COBE* Ref. Pub. No. 95-A (Greenbelt, MD: NASA/GSFC) [DIRBE Exp. Supp.]
- Dube, R. R., Wickes, W. C., Wilkinson, D. T. 1979, ApJ, 232, 333
- Dwek, E. et al. 1998, ApJ, 508, 106
- Dwek, E. & Arendt, R. G. 1998, ApJ, 508, L9

- Eales, S. et al. 1999, ApJ, 515, 518
- Fabian, A. C., astro-ph/9908064
- Fabian, A. C., & Iwasawa, K. 1999, MNRAS, 303, L34
- Ferrara, A., Ferrini, F., Franco, J., & Barsella, B. 1991, ApJ, 381, 137
- Finkbeiner, D. P., Davis, M., & Schlegel, D. J. 1999, ApJ, 524, 867
- Fixsen, D. J., Dwek, E., Mather, J. C., Bennett, C. L., & Shafer, R. A. 1998, ApJ, 508, 123
- Gammie, C. F. 1999, ApJ, 522, L57
- Genzel, R. et al. 1998, ApJ, 498, 579
- Gorjian, V., Wright, E. L., & Chary, R. R. 1999, astro-ph/9909428
- Guiderdoni, B., Bouchet, F. R., Puget, J.-L., Lagache, G., Hivon, E. 1997, Nature, 390, 257
- Haffner, L. M., Reynolds, R. J., & Tufte, S. L. 1998, ApJ, 501, L83
- Harwit, M. 1970, Rivista Del Nuovo Cimento, vol II, 253
- Harwit, M., Protheroe, R. J., & Biermann, P. L., ApJ *in press*; astro-ph/9908338
- Hauser, M. G. et al. 1998, ApJ, 508, 25
- Heiles, C., Haffner, L. M., & Reynolds, R. J. in “New Perspectives on the Interstellar Medium” ASP Conf. Ser. 168, 1999; eds. Taylor, A. R., Landecker, T. L., & Joncas, G.
- Howk, J. C. 1999, astro-ph/9910092
- Hughes, D. et al. 1998, Nature, 394, 241
- Kelsall, T. et al. 1998, ApJ, 508, 44
- Kaufman, M. 1976, Ap&SS, 40, 469
- Kifune, T. 1999, ApJ, 518, L21
- Konopelko, A. K., Kirk, J. G., Stecker, F. W., & Mastichiadis, A. 1999, ApJ, 518, L13
- Lagache, G., Haffner, L. M., Reynolds, R. J., & Tufte, S. L. 1999, astro-ph/9911355
- Low, F., & Tucker, W. 1968, Phys. Rev. Lett., 21, 1538

- Lutz, D., Spoon, H. W. W., Rigopoulou, D., Moorwood, A. F. M., & Genzel, R. 1998, *ApJ*, 505, L103
- Magorrian, J. et al. 1998, *AJ*, 115, 2285
- Malkan, M. A. & Stecker, F. W. 1998, *ApJ*, 496, 13
- Mannheim, K. 1999, *Aph*, 11, 49
- Mushotzky, R. F., Cowie, L. L., Barger, A. J., Arnaud, K. A. 2000, *Nature* (submitted)
- Partridge, R. B., & Peebles, P. J. E. 1967, *ApJ*, 148, 377
- Peebles, P. J. E. 1969, *Phil Trans. Royal Soc. London, A*, 264, 279
- Pozzetti, L., Madau, P., Zamorani, G., Ferguson, H. C., & Bruzual A. G. 1998, *MNRAS*, 298, 1133
- Puget, J. L. et al. 1996, *A&A*, 308, L5
- Puget, J. L. et al. 1999, *A&A*, 345, 29
- Rice, W. et al. 1988, *ApJS*, 68, 91
- Rieke, G. H., Young, E. T., Rivlis, G., & Gautier, T. N. 1996, *AAS*, 189, 309
- Samuelson, F. W. et al. 1998, *ApJ*, 501, L17
- Sanders, D. B., & Mirabel, I. F. 1996 *ARA&A*, 34, 749
- Schlegel, D. J., Finkbeiner, D. P., & Davis M. 1998, *ApJ*, 500, 525
- Smail, I., Ivison, R. J., & Blain, A. W. 1997, *ApJ*, 490, L5
- Soifer, B. T. et al. 1999, astro-ph/9911045
- Soifer, B. T., & Neugebauer, G. 1991, *AJ*, 101, 354
- Stecker, F. W. & de Jager, O. C. 1998, *A&A*, 334, L85
- Taylor, J. H., Manchester, R. N. & Lyne, A. G. 1993, *ApJS*, 88, 529
- Williams, R. E. 1996, *AJ*, 112, 1335
- Zaritsky, D. 1994, *AJ*, 108, 1619

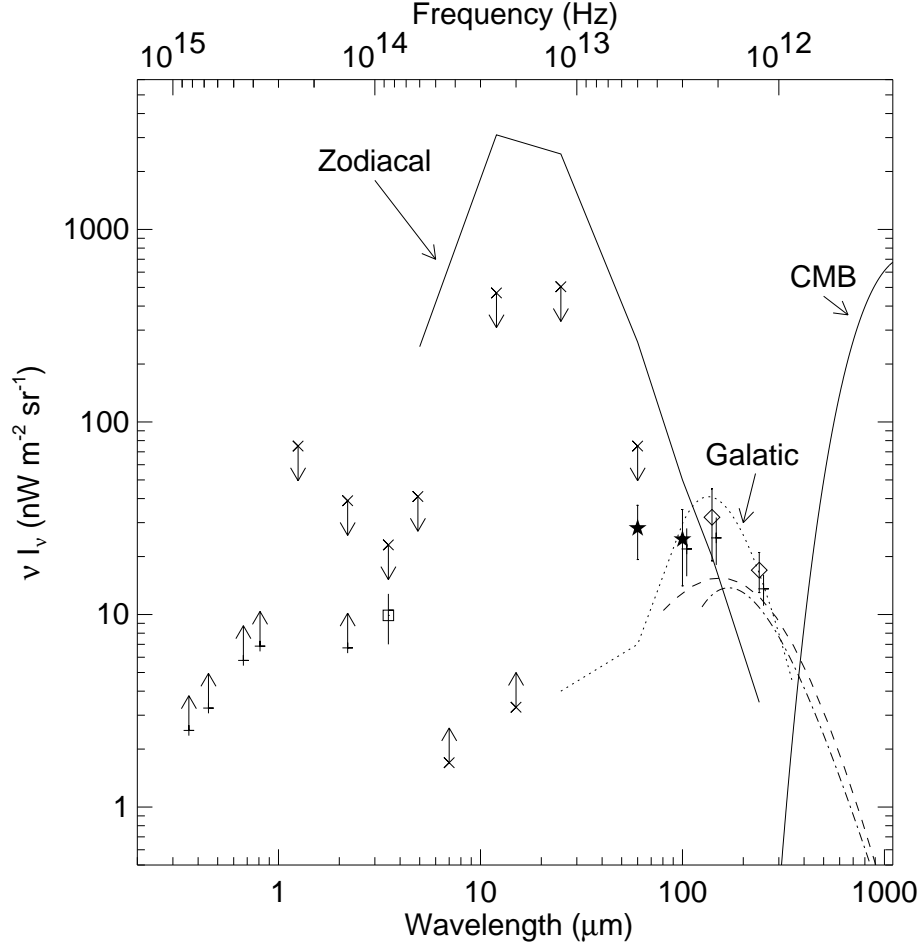


Fig. 1.— Background radiation from UV to submillimeter wavelengths. Lower limits (HST; Pozzetti et al. 1998); square (DIRBE; Dwek & Arendt 1998); lower limits (ISO; Altieri et al. 1999); upper limits (DIRBE; Hauser et al. 1998); diamonds (DIRBE; SFD98); crosses (DIRBE; Hauser et al. 1998); dash-dot line (FIRAS; Fixsen et al. 1998). The filled stars are DIRBE measurements presented in this work. In all cases lower limits are derived from direct number counts, while upper limits and measurements are obtained by subtracting all known foregrounds from the observed sky surface brightness. The dashed line is a simple model motivated by Blain et al.(1999a). The CMBR is shown as a thick line. Typical high-latitude ISM brightness is shown by a dotted line, and approximate IPD brightness at ecliptic poles is a thin line.

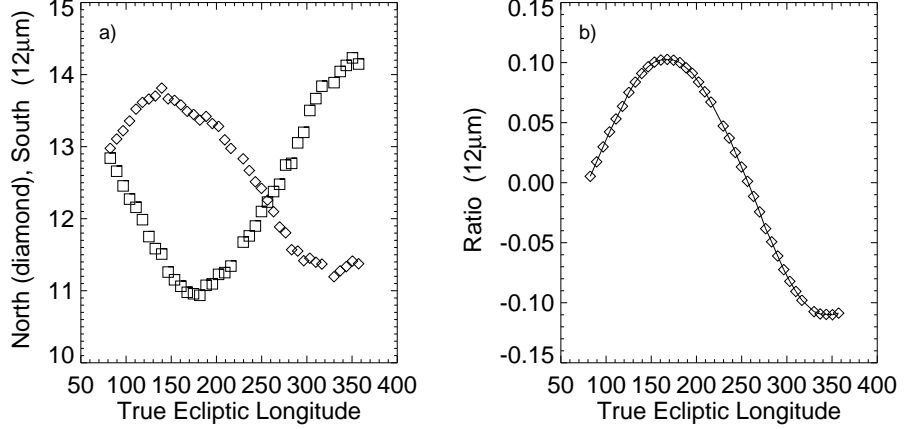


Fig. 2.— Weekly $12\mu\text{m}$ DIRBE data at the ecliptic poles. (a) Weekly flux at the north (diamonds) and south (squares) ecliptic poles in MJy sr^{-1} , plotted as a function of the true heliocentric ecliptic longitude of Earth. (b) The dimensionless ratio of $(N - S)/(N + S)$ defined in eq. (2).

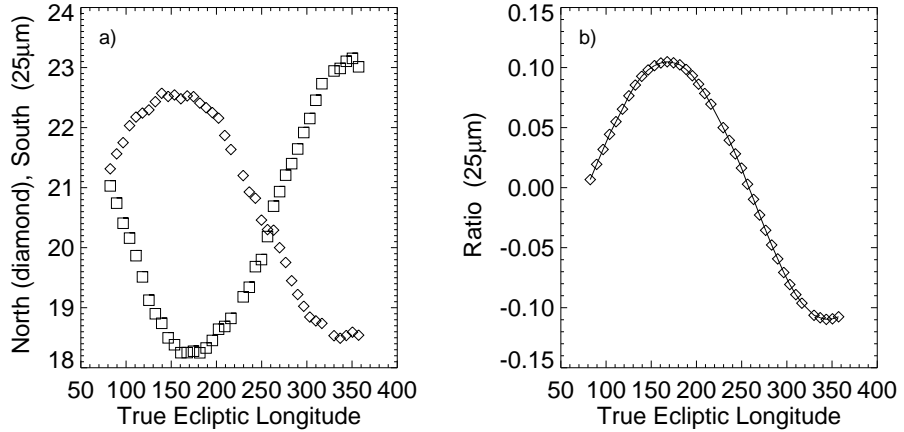


Fig. 3.— Weekly $25\mu\text{m}$ DIRBE data at the ecliptic poles. (a) Weekly flux at the north (diamonds) and south (squares) ecliptic poles in MJy sr^{-1} , plotted as a function of the true heliocentric ecliptic longitude of Earth. (b) The ratio of $(N - S)/(N + S)$ defined in eq. (2).

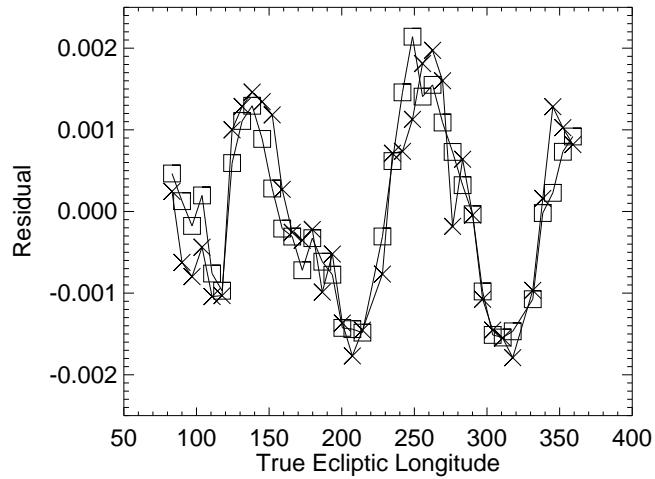


Fig. 4.— Model Residuals difference for $12\mu\text{m}$ (diamonds) and $25\mu\text{m}$. A significant correlation is present in the residuals, but at a level of approximately one part in 1000 of the total signal. The interplanetary dust cloud may not be any smoother than this.

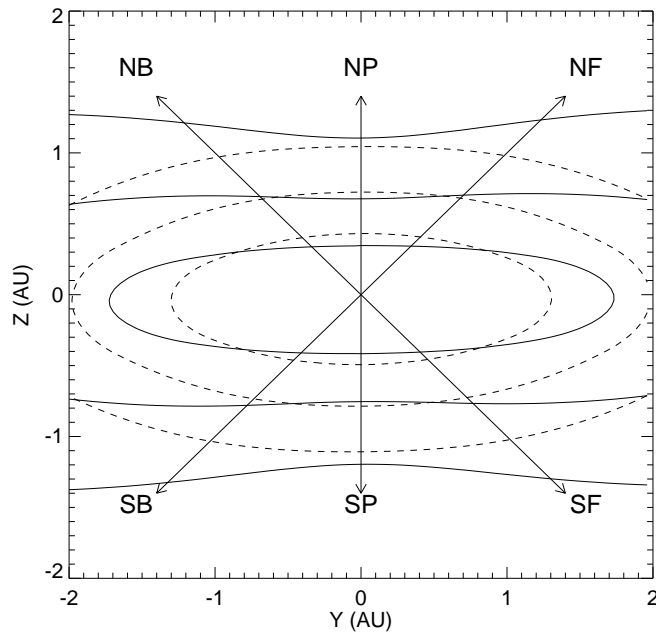


Fig. 5.— Emissivity contours for $12\mu\text{m}$ (dashed) and $240\mu\text{m}$ (solid). The lines of sight used to define Ξ in Eq. (23) are labeled. Earth is located in the middle of the plot, and the Earth-Sun line goes into the page. From this diagram, it is clear that Ξ is larger for longer wavelengths.

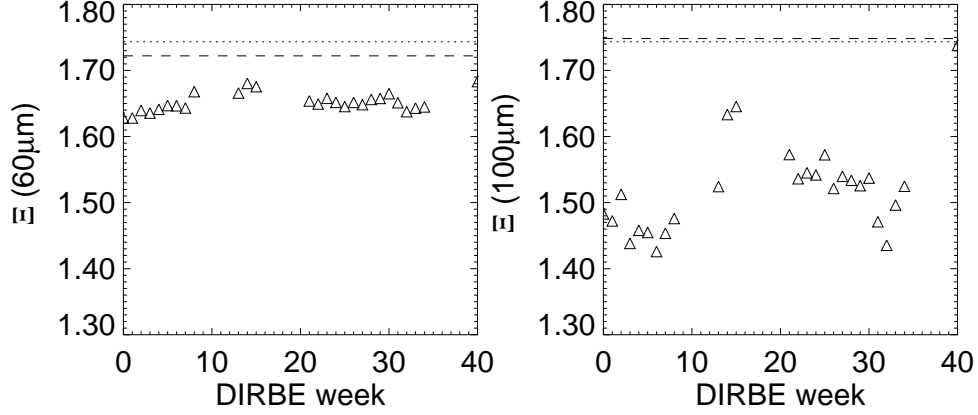


Fig. 6.— Plots of $\Xi(\beta = 35^\circ)$, as defined in eq. (23). In the absence of a CIB signal, these measurements would agree with Ξ_0 from the Kelsall model (*dashed line*). A $\csc|\beta|$ (slab) model is overplotted for comparison (*dotted line*). Plots for other values of β are qualitatively similar.

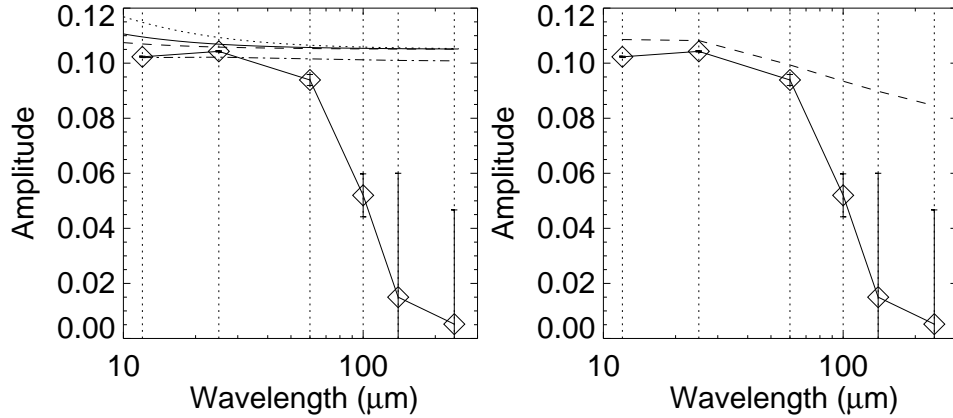


Fig. 7.— Predictions of A . Diamonds are measured amplitudes A' shown in Table 1 with 1 sigma error bars. These amplitudes are approximately the ratio of emission near the ecliptic plane to the total emission - and are therefore nearly model-independent. a) The solid curve is the theoretical A for the widened fan model with $T_0 = 286$ K, dashed line is a factor of 2 warmer dust and dotted line is factor of 2 colder. Also shown is the prediction of the Kelsall et al. model (*dot-dashed line*). b) Two component model. Diamonds are measured amplitudes A' as in previous figure. Dashed line corresponds to a contrived two-component dust model as described in the text. Even in this extreme case, the model prediction cannot be made to agree with the observation at $100\mu\text{m}$.

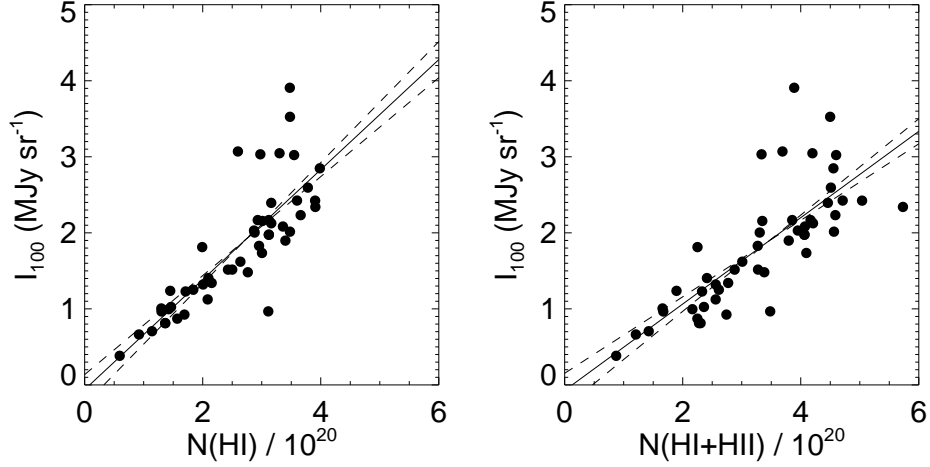


Fig. 8.— The dust/H correlation along the lines of sight to 50 high latitude pulsars ($|b| > 20$, $z > 400$ pc). Formal $\pm 1\sigma$ errors are shown by the dashed lines. a) Dust vs. $N(\text{HI})$. b) Dust vs. $N(\text{H})$. $N(\text{HII})$ derived from pulsar DMs is added to $N(\text{HI})$.

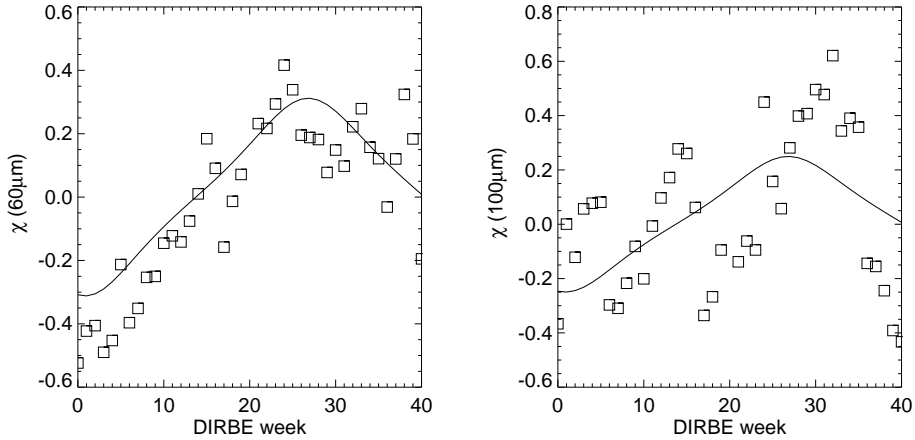


Fig. 9.— Test for $\text{csc } |b|$ slab of dust. (a) Observed value of χ at $60\mu\text{m}$ as defined in eq. (27). The solid line is the χ predicted from a $\text{csc } |b|$ model. (b) χ at $100\mu\text{m}$.

Table 1. CIB Results: Method I

λ (μm)	A' ($\times 10^{-4}$)	ν_0 (deg)	C ($\times 10^{-3}$)	I ($\text{nWm}^{-2}\text{sr}^{-1}$)	B_N ($\text{nWm}^{-2}\text{sr}^{-1}$)	B_S ($\text{nWm}^{-2}\text{sr}^{-1}$)
5	$947. \pm 14.6$	-14.9 ± 0.8	-6.9 ± 1.0	492.8	21.0 ± 3.7	24.4 ± 3.7
12	$1023. \pm 2.5$	-26.9 ± 0.1	-1.6 ± 0.2	6214.2	55.5 ± 7.9	65.2 ± 7.9
25	$1043. \pm 2.6$	-25.6 ± 0.1	-0.6 ± 0.2	4930.9	-1.0 ± 6.7	2.0 ± 6.7
60	$939. \pm 19.8$...	-3.3 ± 1.4	583.2	28.1 ± 5.9	30.0 ± 5.9
100	$520. \pm 78.3$...	1.0 ± 5.8	161.4	40.5 ± 6.5	40.4 ± 6.5
140	$150. \pm 451.5$...	7.5 ± 31.4	85.5	36.9 ± 19.9	36.3 ± 19.9
240	$52. \pm 414.5$...	7.8 ± 28.8	30.8	14.8 ± 6.6	14.5 ± 6.6

Note. — Fit parameters described in the text. A' is the amplitude of the annual variation in the dimensionless ratio R . The ascending node true anomaly, ν_0 , is fit for 12 and $25\mu\text{m}$, and forced to be $\nu_0 = -25.0^\circ$ for the other wavebands for fit stability. C is the mean value of R averaged over an entire cycle. I is the total emission at the poles ($B + Z$). Values of B_N and B_S (excess at north and south ecliptic poles) are shown separately to demonstrate that the model is robust with respect to a $N - S$ difference in the cirrus.

Table 2. CIB Results: Method II

β (deg)	$\csc \beta$	$\Xi_{K_{60}}$	Ξ_{60}	$B_{60}/2$ (nW m ⁻² sr ⁻¹)	$\Xi_{K_{100}}$	Ξ_{100}	$B_{100}/2$ (nW m ⁻² sr ⁻¹)
35	1.743	1.722	1.649	29.3 ± 2.9	1.748	1.524	23.4 ± 3.7
40	1.556	1.553	1.501	27.2 ± 3.3	1.571	1.416	21.2 ± 5.3
45	1.414	1.419	1.378	28.1 ± 4.9	1.432	1.312	21.6 ± 6.7
50	1.305	1.312	1.285	25.5 ± 5.5	1.321	1.279	10.3 ± 12
Ave				28.0 ± 1.9			21.9 ± 2.7

Note. — The results of Method II. Col. (1): ecliptic latitude, β . Col. (2) $\csc \beta$ - the value of Ξ in the case of a uniform slab of dust (see eq. [23]). Col. (3): Ξ_K - the value of Ξ at $60\mu\text{m}$ expected for the Kelsall model and no background. Col. (4): Observed value of Ξ at $60\mu\text{m}$. Col. (5): Intensity of background derived from Ξ_{60} (eq. [25]). Col. (6-8): same as col. (3-5) but for $100\mu\text{m}$.

Table 3. Method II Model Dependence

Par	value	σ	Δ_{60} (%)	Δ_{100} (%)	$\Delta_{60}(3\sigma)$ (%)	$\Delta_{100}(3\sigma)$ (%)
Ω (deg)	77.7	0.600	0.013	0.005	0.040	0.013
i (deg)	2.03	0.0170	0.001	0.002	0.005	0.005
α	1.34	0.0220	5.533	2.042	16.310	6.012
n_0 (AU ⁻¹)	1.13×10^{-7}	6.40×10^{-10}	0.020	0.009	0.058	0.027
δ	0.467	0.00410	1.938	0.576	5.782	1.720
T_0 (K)	286.	5.00	1.501	0.305	4.364	0.886

Note. — Dependence of IR excess measurements on Kelsall model parameters. The very weak dependence shown here indicates that either the Kelsall model does not contain the necessary freedom to adequately describe the zodiacal emission, or else there is a time-independent component that accounts for the IR excess.

Table 4. Systematic Errors

Reason	Meth I Δ_{60} (nW m ⁻² sr ⁻¹)	Meth I Δ_{100} (nW m ⁻² sr ⁻¹)	Meth II Δ_{60} (nW m ⁻² sr ⁻¹)	Meth II Δ_{100} (nW m ⁻² sr ⁻¹)
Model	5	5	3	1
Algorithmic	7	11	2	6
IR Excess Total	12	16	5	7

Note. — Summary of systematic uncertainties. Model errors reflect the dependence of the IR excess on IPD model parameters. Algorithmic errors refer to uncertainty caused by the details of the implementation of each method. The sum of these errors is the systematic uncertainty in the measured IR excess – errors that average down when results from the two methods are combined. Additional systematic uncertainty results from the WIM and WNM subtraction; these errors do not average down and are included in Table 6. All errors are 95% confidence.

Table 5. Bad Pixels and Weeks

λ (μm)	Pixels Used %	No. Weeks
4.9	-	39
12	79	39
25	80	39
60	55	39
100	46	31
140	82	41
240	83	41

Note. — Column (1), DIRBE waveband. Col. (2) fraction of pixels used in all good weeks. Col. (3) Number of good weeks out of 41 science weeks in the DIRBE mission. The $100\mu\text{m}$ channel has a large number of weeks discarded due to hysteresis effects near the north ecliptic pole. This effect is also present, but much smaller at $60\mu\text{m}$.

Table 6. Final results

	60 μm (nW m ⁻² sr ⁻¹)	100 μm (nW m ⁻² sr ⁻¹)	140 μm (nW m ⁻² sr ⁻¹)	240 μm (nW m ⁻² sr ⁻¹)
Method I	29.0 ± 5.9 ± 6	40.4 ± 6.5 ± 8	36.6 ± 19.9	14.6 ± 6.6
Method II	28.0 ± 1.9 ± 3	21.9 ± 2.7 ± 4
Mean	28.1 ± 1.8 ± 3	24.6 ± 2.5 ± 4
WIM/CNM	4	4
Recommended	28.1 ± 1.8 ± 7	24.6 ± 2.5 ± 8	25.0 ± 6.9	13.6 ± 2.5

Note. — Summary of results. In cases where two errors are shown, the first is statistical and the second is systematic. All errors are 1σ . Recommended values for 140 and 240 μm are taken from Hauser et al. (1998).